Anisotropic magnetic behavior in Dy/Y films and superlattices

F. Tsui, C. P. Flynn, and M. B. Salamon
Department of Physics and Materials Research Laboratory, University of Illinois at Urbana-Champaign, 1110 West Green Street, Urbana, Illinois 61801

R. W. Erwin, J. A. Borchers, and J. J. Rhyne
National Institute of Standards and Technology, Gaithersburg, Maryland 20899
(Received 26 November 1990)

By neutron diffraction we show that superlattices of Dy and Y grown by molecular-beam epitaxy along the hcp *b* axis exhibit little magnetic coupling between successive Dy layers, even for Y spacers as thin as 9 atomic planes (26 Å). Previous studies of Dy/Y superlattices grown along the hcp *c* axis established that long-range three-dimensional helimagnetic ordering takes place even through Y spacer layers as thick as 120 Å. This highly anisotropic coupling behavior is shown to have its origin in nearly-two-dimensional nesting features of the Y and Dy Fermi surfaces. Nesting along the *c* axis gives rise to sharp peaks along **c** in the wave-vector-dependent magnetic susceptibility, and causes the exchange coupling to exhibit long-range oscillations in real space. The lack of nesting features along the *b* axis leaves a rapid exponential decay of the exchange interaction with spin separation. From magnetic measurements by superconducting-quantum-interference-device magnetometry on *b*-axis superlattices and films, we deduce that the first-order ferromagnetic transition of Dy is suppressed, and that the critical field required to produce the ferromagnetic alignment is much higher than the *c*-axis counterpart. This difference arises from anisotropy of the energy balance of the system. The magnetic coherence in *b*-axis superlattices and films is anisotropic and exhibits an unusual temperature dependence.

I. INTRODUCTION

Rare-earth (RE) metals and alloys exhibit a rich diversity of magnetic structures.[1] At low temperature they develop magnetization waves with wavelengths of about 9 atomic planes. These arise from the interplay of nearly-two-dimensional (2D) nesting features of the RE Fermi surface (FS) with magnetocrystalline anisotropy.[2] As the temperature is lowered, magnetoelastic driving forces become increasingly important, eventually overcoming the exchange barrier to turn bulk RE's ferromagnetic below a critical temperature T_c. Single-crystal superlattices (SL's) synthesized from heavy RE's and Y have created a new class of 3D magnetic structures[3] and give valuable insight into the origins of the RE magnetic structures. Recent advances in molecular beam epitaxy (MBE) permit the growth of high-quality RE thin films and SL's in chosen orientations and make it possible to undertake studies of the highly anisotropic magnetic structures of heavy RE's.[3–5] The mechanical constraint provided by epitaxy, in particular, alters the magnetoelastic behavior and, consequently, the temperature dependence of the magnetization wavelength. In this paper, we report the results of neutron-diffraction and magnetization measurements on three samples grown by MBE techniques along the hcp *b* axes. Two are Dy/Y SL's: sample *A* is *b*-$[(Dy)_{26}|(Y)_9]_{82}$, with 26 Dy planes and 9 Y planes repeated 82 times, and sample *B* is *b*-$[(Dy)_7|(Y)_{25}]_{67}$. Sample *C* is a 350-Å film of pure Dy grown epitaxially on Y. We refer to samples grown along *b* or *c* axes as *b*-axis and *c*-axis samples, respectively. Our results on *a*-axis samples are very similar to that of the *b*-axis ones, and we will include some of these results, especially interlayer magnetic coherence, in the discussion.

Neutron diffraction experiments on *c*-axis Gd/Y, Dy/Y, Er/Y, and Ho/Y SL's reveal that, although Y has no $4f$ core magnetism, magnetization wave propagate through intervening nonmagnetic Y layers as thick as 120 Å.[3,6] Previous work[3,6] on *c*-axis Dy/Y SL's has shown that the chirality of the Dy helimagnetic spin wave is preserved through many intervening Y layers. This is explained[7] as a consequence of the Ruderman-Kittel-Kasuya-Yosida (RKKY) interaction in which the helical Dy spin wave induces two orthogonal, out-of-phase RKKY components in the Y that together carry circular polarization. In Dy/Y *c*-axis SL's, helimagnetic ordering occurs at about 175 K, close to the value 180 K in bulk Dy. The turn angle ω is about 43° at the Néel point and decreases with temperature to about 30°, depending on the Dy layer thickness. Dilute Dy alloys in Y also exhibit helical waves but the Néel temperature is much lower and the helical turn angle of 50° is much less temperature dependent. The transmission of magnetic coherence through Y layers in SL's does not result from alloying. In fact, detailed structural analysis has shown that the Dy/Y interfaces are fairly sharp.[3] The first-order ferromagnetic transition observed in bulk Dy at 85 K is not observed to 4 K. Instead, a field of several kOe along one of the easy *a* axes is needed to produce ferromagnetism in Dy *c*-axis epilayers, and the transition occurs stepwise

through intermediate states.

In this paper, we report strikingly different magnetic behavior in *b*-axis materials. Such magnetic properties as spin-spin coupling, magnetic coherence, and critical fields and their temperature dependences, show a strong dependence on growth direction. This orientation dependence arises from the highly anisotropic electronic structures of the RE's. Our results offer new insight into the 3D character of magnetic response and the resulting magnetic phase transitions in the heavy RE's. The MBE growth of *a*- and *b*-axes samples requires new procedures. These are outlined in Sec. II, together with the measurements. Three aspects of the experimental results are discussed in Sec. III. The first, the spin-spin coupling through Y layers, and the observed ordering (or lack of it), are reconciled with the known RE electronic structures. We then discuss the magnetic structures, in particular, the phase transitions, and finally turn to the question of intralayer magnetic coherence.

II. EXPERIMENT

A. Crystal growth

An earlier publication reports how *a*- and *b*-axes films and SL's can be grown on single crystals of bulk Y.[4] In the present research, yttrium substrate crystals about 2 mm thick with a surface area of greater than 1 cm^2 were used for neutron scattering, and squares with a surface area ~ 0.1 cm^2 for SQUID measurement. These were obtained from the crystal preparation group at the Ames Laboratory and cut with the *a* or *b* axes perpendicular to the desired growth planes. A high-quality surface was produced by electropolishing the crystals in a perchloric acid and methanol solution.

Yttrium substrates were reelectropolished immediately before being introduced into the MBE chamber. A high-temperature anneal at 750 °C in the chamber produces sharp reflection high-energy electron-diffraction (RHEED) patterns. In order to further reduce surface roughness, about 1000 Å of Y was then deposited at 500 °C, prior to actual SL growth. Interdiffusion, which is known to be anisotropic in the hcp RE metals,[8] was minimized in the SL by maintaining the growth temperature at 350 °C, which is 50 °C lower than that used for *c*-axis SL's. Thin films were generally grown at ~ 400 °C because the higher temperatures resulted in a smoother growth.

RHEED observation made during annealing and growth revealed a variety of temperature-dependent surface reconstructions of the *b* face. In general, the RE surfaces appear to prefer closed-packed arrangements. On the *b* face, only the "closed-packed" $[1\bar{2}10]$ direction remains ordered, with the non-closed-packed directions disordered. Similar behavior is also observed in other systems such as noble-metal (100) surfaces.[9] This transformation occurs when the energy gained by surface contraction exceeds the energy lost by lack of registry with the underlying atomic layers. We find that, when each surface layer is buried at normal growth rates, the reconstruction is relieved and the atoms revert to bulk registry, so that crystals with excellent 3D order are obtained.

The 1D surface order gives rise to "sheets" in reciprocal space in place of the normal termination "rods" of a 2D ordered surface. RHEED diffraction appears as rings along the ordered direction, highly elongated streaks perpendicular to it, and arched streaks in between.[10] Figure 1(a) shows RHEED patterns for one such surface. At high growth temperature, or after annealing, the surfaces exhibited 1D order, although x-ray diffraction on the resulting film revealed a high-quality 3D order, as mentioned above. Figure 1(b) shows the RHEED patterns of an unreconstructed *b* face grown at low temperature (≤ 350 °C) at a low growth rate (< 0.3 Å/sec). Such patterns were also observed during higher-temperature annealing at ~ 750 °C. Under these conditions, the bulk driving force apparently becomes stronger than the surface interactions that produce a high density but partly disordered surface.

A typical x-ray Bragg scan for a *b*-axis SL, sample *A*, is shown in Fig. 2. This demonstrates the quality available in *b*-axis Dy/Y SL's. The Bragg peak widths are $\sim 0.1°$ and the rocking curves are $< 0.3°$. The intensities of several orders of SL sideband surrounding the central Bragg peak indicate that the interdiffusion is limited to about four interface layers, similar to that of the *c*-axis samples. The interface may be somewhat rougher than the *c*-axis counterpart on a lateral scale of 10^3 Å, but the overall quality of the samples remains very good.

B. Neutron scattering

Neutron-scattering experiments were carried out on a triple-axis spectrometer at the National Institute of Standards and Technology Reactor. A graphite analyzer crystal set for zero-energy transfer was used to reject neutrons inelastically scattered by the thick Y substrate. Collimations of 40′-25′-25′-40′ resulted in a resolution of 0.02 $Å^{-1}$ for longitudinal scans and 0.008 $Å^{-1}$ for trans-

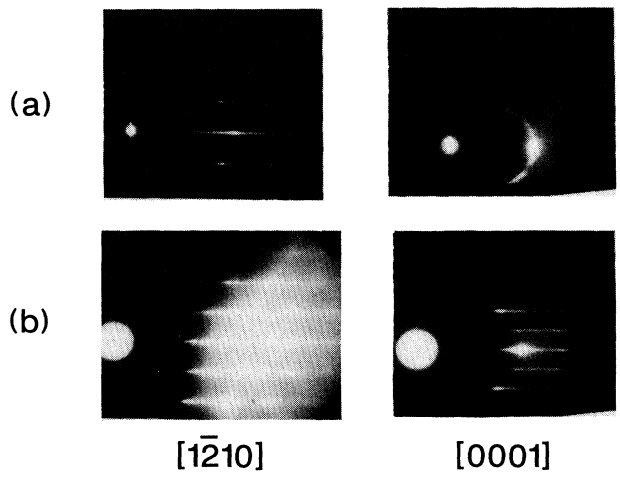

FIG. 1. Typical RHEED pictures for *b*-axis samples: (a) a reconstructed surface showing long streaks along the $[1\bar{2}10]$ azimuth and an arc along the [0001] azimuth, and (b) an unreconstructed surface having somewhat shorter streaks along both $[1\bar{2}10]$ and [0001] directions.

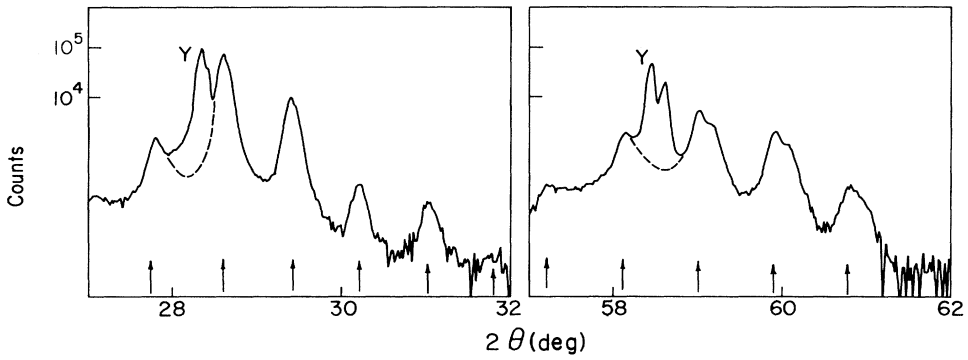

FIG. 2. X-ray Bragg scan along **b** on sample A near $(10\bar{1}0)$ and $(20\bar{2}0)$. Arrows indicate the superlattice sidebands.

verse scans. Our measurements were designed to probe the magnetic structure, the coherence between and in the individual Dy layers, and the temperature dependence of the order.

A basal plane spiral with wave vector $\mathbf{q}_0=\kappa\mathbf{c}^*$ along $\mathbf{c}^*$ gives rise to magnetic satellites at $(0\,0\,0\,2\pm\kappa)$. Interlayer magnetic coherence along **b** can be examined by scanning across the magnetic satellites along the growth direction in a $(\zeta\,0\,\bar{\zeta}\,2\pm\kappa)$ scan, with ζ the scan variable. As an example, Fig. 3 shows one such scan for sample A at 6 K with $\kappa=0.204$ and $c^*=1.111$ Å^{-1}.

The nuclear SL peak width Δ was determined from the structural Bragg peaks at $(\delta 0\bar{\delta}2)$ with $\delta=2\pi/La^*$, where L is the SL period, and $a^*=1.99$ Å^{-1}. To increase the scattering contrast with the Y layers, a 2.5-T magnetic field was applied in the growth plane, along the easy $[1\bar{2}10]$ direction of magnetization, in order to drive the Dy layers ferromagnetic. These $(\delta 0\bar{\delta}2)$ scans are superimposed on the magnetic satellite in Fig. 3. The full width of the structural satellites is $\Delta=0.017$ Å^{-1} with an instrumental resolution of 0.008 Å^{-1}. Because the ferromagnetic coherence extends over the entire sample, Δ measures the mosaic width and the structural regularity of the SL. From the full width $\Delta Q_{a^*}=0.078$ Å^{-1} of the magnetic peak and the measured intrinsic width of $\Delta=0.017$ Å^{-1} for the nuclear Bragg peaks, we estimate the coherence length along the growth axis for sample A to be

$$\xi_b=2\pi/[(\Delta Q_{a^*})^2-\Delta^2]^{1/2}\sim 80\ \text{Å}\ . \tag{1}$$

In Eq. (1) we have approximately deconvoluted the observed widths to obtain the magnetic coherence length ξ_b.

The magnetic coherence lengths along the b-axis growth direction are 80 and 40 Å for samples A and B, respectively. When these are compared with the Dy layer thickness of 73 and 20 Å for the two samples, the magnetic coherence is seen to be confined mainly to a single Dy layer. Interlayer magnetic coupling appears to be small or negligible for Y spacer layers as thin as 9 atomic planes. As an example, the inset in Fig. 3 is a $(0\,0\,0\,2+\zeta)$ scan along the growth direction on a c-axis SL similar to sample A which shows that the magnetic coherence length of a typical c-axis SL is ≥ 500 Å, corresponding to many SL periods.

Although no interlayer ordering occurs in the b-axis SL's, each Dy layer remains magnetically coherent below T_N. As explained above, the coherence length ξ_b along the $[10\bar{1}0]$ direction is temperature independent at approximately the layer thickness. The widths of the magnetic peaks along the $[1\bar{2}10]$ direction are also observed to be temperature independent and comparable in size to Δ. They correspond to long-range magnetic coherence along **a** with $\xi_a\geq 500$ Å. In contrast to this behavior, the coherence length ξ_c along **c** is found to be surprisingly small and to *decrease* with temperature. This curious

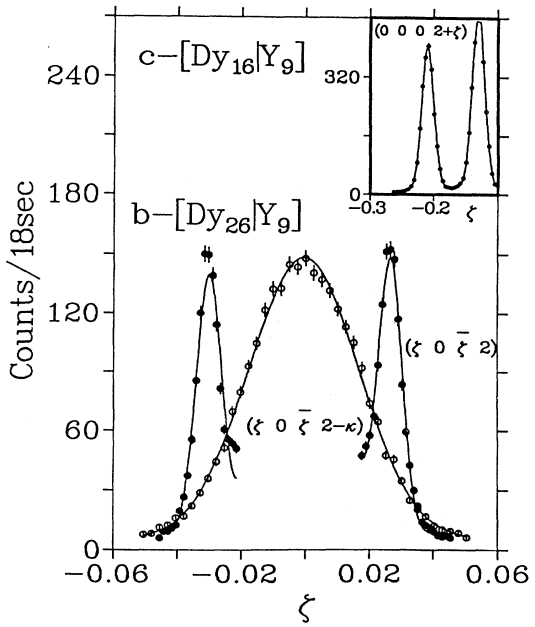

FIG. 3. Neutron diffraction from the b-axis SL $[(Dy)_{26}|(Y)_9]$ (sample A). Open circles, scan along $\mathbf{a}^*$ across the $(0\,0\,0\,2-\kappa)$ magnetic peak; solid circle, scan through the (0002) structural peak along $\mathbf{a}^*$ in a field of 2.5 T to show the structural satellites of (0002). After Ref. 5.

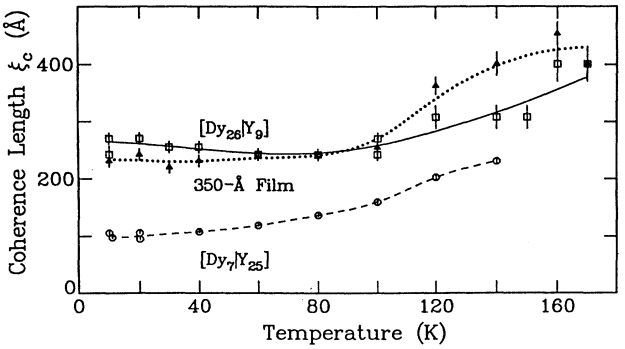

FIG. 4. Temperature dependence of the magnetic coherence along c (Ref. 5). The coherence length along $[1\bar{2}10]$ is comparable to the structural coherence and independent of temperature.

temperature dependence has not been observed in other RE SL's but occurs in all *a*- and *b*-axes samples. ξ_c is shown as a function of temperature in Fig. 4. The coherence points to a quasi-2D magnetic structure comprised of ferromagnetic sheets in the *a*-*b* plane, extending throughout each Dy layer, but stacked in a spiral along the *c* axis that is coherent only over this short, temperature-dependent domain size.

C. Magnetic behavior

Bulk magnetic properties were measured on 0.1-cm^2 square samples using a commercial SQUID magnetometer. The field was applied in growth plane along the $[1\bar{2}10]$ direction. The presence of the thick Y substrate (2 mm) required that careful measurement of the background substrate susceptibility be made. Figure 5 shows the temperature dependence of the substrate magnetization in a 2-kOe field. It exhibits a gradual linear rise at high temperature identical to that of pure Y,[11] and a typical Curie-law addition near 0 K due to impurities. The unusual peak at ~60 K, not found in the literature, evidently arises from other unidentified magnetic impurities. The susceptibility is isotropic and its field dependence is

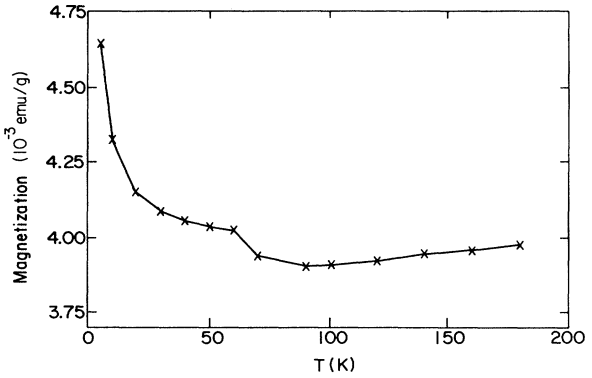

FIG. 5. The magnetization curve with a field of 2 kOe for the single-crystal Y substrates used in the *a*- and *b*-axes samples.

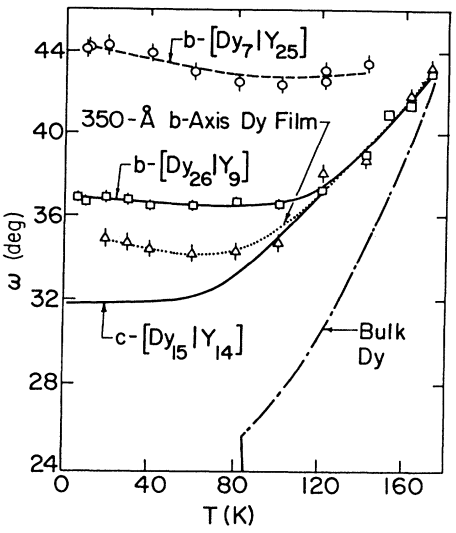

FIG. 6. Temperature dependence of the helimagnetic turn angle ω for *b*-axis samples, for the *c*-axis SL *c*-$[(DY)_{15}|(Y)_{14}]$, and for bulk Dy.

that of a paramagnet with a small ferromagnetic bias:

$$M=\chi H+M_0 \ . \tag{2}$$

The susceptibility of the film is then obtained by subtracting off the substrate contribution in proportion to its mass.

The magnetic structures of the *a*- and *b*-axis Dy layers differ from that of bulk Dy. A helimagnetic transition occurs in samples *A* and *C* at $T_N \sim 175$ K and for sample *B* with $T_N \sim 150$ K. The helimagnetic turn angle ω ($=\pi\kappa$) determined by neutron scattering has a much weaker temperature dependence than either bulk Dy or comparable *c*-axis SL's (see Fig. 6). The first-order ferromagnetic transition, which occurs in the bulk at $T_c = 85$ K, is completely suppressed in these samples. As in *c*-axis samples, the temperature dependence of the magnetization shows strong hysteresis between field-cooled and zero-field-cooled states. A typical magnetiza-

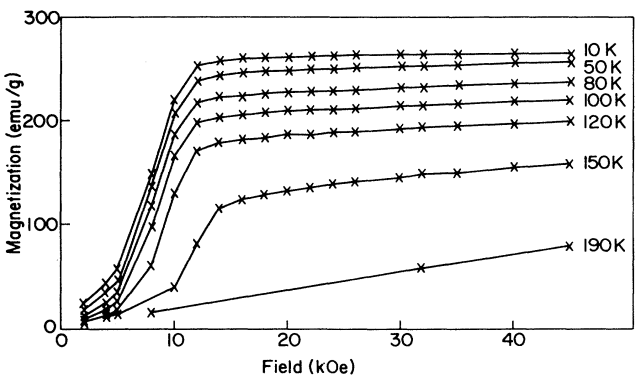

FIG. 7. Field-dependent magnetization curves for the field-cooled *b*-axis SL $b-[(Dy)_{26}|(Y)_9]$ (sample *A*).

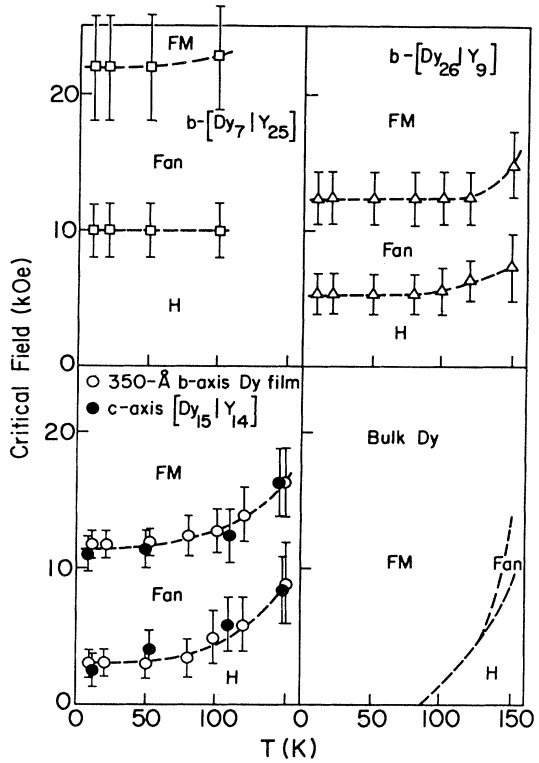

FIG. 8. Variation of critical fields H_c and H_f with temperature for the b-axis samples, for a c-axis SL c-$[(Dy)_{15}|(Y)_{14}]$, and for bulk Dy. Below H_c the sample is in the helimagnetic phase and above H_f it is in the ferromagnetic state; between H_c and H_f, the sample is in a "fan" state.

tion curve as a function of applied field for field-cooled sample A is shown in Fig. 7. The changes of slope visible in Fig. 7 indicate the presence of an intermediate "fan" state. The first feature at low field, corresponding to the critical field H_c, marks the initial collapse of the helical waves. Neutron-diffraction data indicate that a weakening helimagnetic scattering occurs well below the low-field anomaly. The second notable feature, at higher field is the final saturation at a field H_f. The observed H_c and H_f are both shown in Fig. 8. In comparison with bulk Dy samples and with c-axis Dy/Y SL's such as c-$[(Dy)_{15}|(Y)_{14}]_{64}$, also shown in Fig. 8, the b-axis samples require a larger H_c and H_f at low temperature. The strong dependence on both the crystal orientational and the epilayer thickness suggests that lattice clamping plays a major role.

III. DISCUSSION

A. Interlayer magnetic coupling

The a- and b-axis SL's fail to develop 3D magnetic ordering even for Y spacers as thin as 26 Å. Magnetic coherence is thus confined mainly to individual Dy layers, as discussed in Sec. II A. On the other hand, c-axis SL's maintain magnetic coherence, including the chirality of the helix, through many SL bilayers and for Y layer thickness up to 120 Å (Ref. 6).

This highly anisotropic dependence of coupling on growth orientation can be understood qualitatively by studying the magnetic response of two magnetic ions in a Y lattice. Two ions with spins $\mathbf{S}_1,\mathbf{S}_2$ at positions $\mathbf{r}_1$ and $\mathbf{r}_2$ are coupled through the Y conduction electrons by a Hamiltonian $\mathcal{H}=-J(\mathbf{R})\mathbf{S}_1\cdot\mathbf{S}_2$, where the separation is $\mathbf{R}=\mathbf{r}_2-\mathbf{r}_1$ and the real-space exchange coupling $J(\mathbf{R})$ is the Fourier transform of $j(\mathbf{q})$,[1,2] namely,

$$J(\mathbf{R})=\sum_{\mathbf{q}} j(\mathbf{q})\exp(-i\mathbf{q}\cdot\mathbf{R}) . \tag{3}$$

Second-order perturbation theory gives $j(\mathbf{q})=|j_{sf}(\mathbf{q})|^2\chi(\mathbf{q})$, with $j_{sf}(\mathbf{q})$ the exchange matrix element connecting band states to the $4f$ core, and $\chi(\mathbf{q})$ the generalized susceptibility. The magnetic moments perturb the Y conduction electrons through this $\mathbf{q}$-dependent linear response function $\chi(\mathbf{q})$. For an isotropic electron gas, $\chi(\mathbf{q})$ is isotropic and $J(\mathbf{R})$ takes the well-known RKKY form

$$\sim\cos(2k_F R)/(k_F R)^3 .$$

In the case of hcp RE's, $J(\mathbf{R})$ is not isotropic, and its symmetry plays an essential role in determining how the spins coupled with each other.

For Dy and Y, $j(\mathbf{q})$ along $\mathbf{c}^*$ has been modeled and measured by various methods in past work.[1] There are well-known peaks at nonzero $\mathbf{q}$ that arise from nearly 2D nesting features in the hole FS at the wave vectors $\mathbf{q}_0$ that span these 2D sheets. These features reflect a near instability of the electron liquid to the formation of a spin-density wave characterized by $\mathbf{q}_0$. In contrast, the exchange matrix element $j_{sf}(\mathbf{q})$ is nearly isotropic and almost the same for all heavy RE's.[12–14] It decreases with q and has a width corresponding inversely to the size of the $4f$ shell. Less is known about the behavior along $\mathbf{a}^*$ and $\mathbf{b}^*$, but, because of the flatness of the 2D sheets, we assume that $j(\mathbf{q})$ falls off with q like $|j_{sf}(\mathbf{q})|^2$, and may reasonably be represented by a Gaussian of width 0.6 $Å^{-1}$ (Ref. 14). A sketch showing general features of $j(\mathbf{q})$ is given in Fig. 9(a). The envelope of $J(\mathbf{R})$, consistent with Fig. 9(a), is sketched in Fig. 9(b). The peaks in $j(\mathbf{q})$ along $\mathbf{c}^*$ give rise to oscillations of wave vector $\mathbf{q}_0$ in $J(\mathbf{R})$. As shown in Fig. 9(b), they decay with a range inversely proportional to the peak widths of $j(\mathbf{q})$. Along $\mathbf{a}^*$ and $\mathbf{b}^*$, the broad width of $j(\mathbf{q})$ causes a rapid exponential decay of $J(\mathbf{R})$. This anisotropy is qualitatively consistent with our observation of the magnetic coupling range in the SL's.

To model the c-axis oscillations quantitatively, a more detailed $\chi(\mathbf{q})$ is needed. Peaks in $\chi(\mathbf{q})$ for Dy and Y are thought to differ in $\mathbf{q}_0$ values, peak heights, and widths in order to account for the observed differences in spin-wave vectors, mean free paths, etc., of the pure metals.[13] The present discussion is idealized to treat Dy local moments as if they were isolated in Y, for which only the conduction electrons of Y are involved. Thus, only $\chi(\mathbf{q})$ for Y is needed. Equivalently, $\chi(\mathbf{q})$ may be considered identical for Dy and Y and, in point of fact, Dy and Y do have

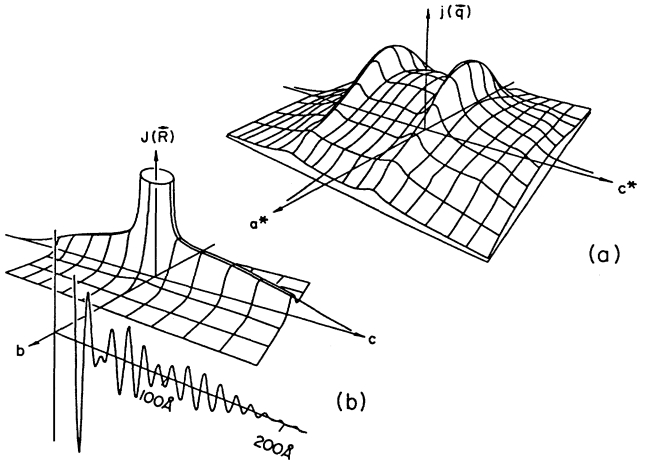

FIG. 9. (a) Schematic representation of $j(\mathbf{q})$. (b) The envelope function of the Fourier transform of $j(\mathbf{q})$ in (a) shows the spatial anisotropy. Inset in the foreground is the actual Fourier transform $J(\mathbf{R})$ using Liu's $\chi(\mathbf{q})$ along **c** (Ref. 13). After Ref. 5.

similar $\chi(\mathbf{q})$. Indeed, greater differences exist amongst different calculations for a single metal than between the two metals, owing to the complexity of the electronic structures in RE's.[13,14] The most detailed $\chi(\mathbf{q})$ available for Y was calculated by Liu *et al.*[13] They found a peak $\sim 0.7\chi(0)$ high, with a markedly square top, containing sharp structure of width ~ 0.03 Å^{-1}. We have fitted this peak with a superposition of several Gaussian components ~ 0.03 Å^{-1} wide to reproduce their $\chi(q)$. When multiplied by the matrix element and Fourier transformed, this gives the $J(\mathbf{R})$ shown in Fig. 9(b). The Gaussian fit has an advantage over a numerical transformation in that artificial oscillations are naturally avoided. The resulting $J(\mathbf{R})$ exhibits long-range oscillations along **c** which extend more than 100 Å, with beats that result from the sharp features of $\chi(\mathbf{q})$. Perpendicular to **c**, the lack of narrow features in **q** causes $J(\mathbf{R})$ to fall off 1 order of magnitude faster.[14]

To obtain the total coupling energy between layers of moments, the interactions must be summed over all pairs. Model calculations of this type have been performed by Yafet and co-workers.[7] Various uncertainties that remain in the present knowledge of $j(\mathbf{q})$ limit the quantitative value of the detailed results. For the present we can center our interpretation on the observed anisotropy of $J(\mathbf{R})$ described above, rather than on detailed simulations.

In the real Dy/Y SL's studied here, the magnetic moments are coupled through the conduction electrons of both Y and Dy. Thus, the difference of $\chi(\mathbf{q})$ between the two materials further perturbs the final form of $J(\mathbf{R})$. The materials are not truely homogeneous, since $\chi(\mathbf{q})$ contains the linear responses of both Dy and Y conduction electrons, and the real $J(\mathbf{r}_1,\mathbf{r}_2)$ depends explicitly on both $\mathbf{r}_1$ and $\mathbf{r}_2$ rather than **R** alone. To go beyond the simple model of two ions in the Y matrix in order to account for the lowest-order correction due to $\chi(\mathbf{q})$ differences, we consider RE atomic planes separated by R, embedded in Y in the growth plane, following the treatment by Yafet *et al.*[7] For growth perpendicular to the basal plane, the spatial form along **c** of $J(R)$ stays the same as in Fig. 9(b) because $j(q_{c*})$ sharply peaks at q_0 and

$$J(R)=\sum_{\mathbf{q},R_a,R_b} j(\mathbf{q})\exp(-i\mathbf{q}\cdot\mathbf{R}) = \sum_{q_{c*}} j(0,0,q_{c*})\exp(-iq_{c*}R)\ . \tag{4}$$

On the other hand, if the RE sheet lie in the *a-c* plane, the Dy spins form a spiral with a different wave vector $\mathbf{q}_0'$, and the exchange interaction along **b** is

$$J(R)=\sum_{\mathbf{q},R_a,R_c} j(\mathbf{q})\exp(-i\mathbf{q}\cdot\mathbf{R}+iq_0'R_c) = \sum_{q_{a*}} j(q_{a*},0,q_0')\exp(-iq_{a*}R)\ . \tag{5}$$

In this case, the spatial form along **b** of $J(\mathbf{R})$ again remains the same as in Fig. 9(b), but the summation misses the peak along **c** in $j(q)$ by $\Delta q = q_0 - q_0'$ resulting in an exponential reduction of interlayer exchange. Since the summation extends over q_{a*} [Eq. (5)], this reduction can be factored out of the sum, and for a peak width of D along **c**, its exponent is $-(\Delta q/D)^2$. Therefore, when Δq is large compared to D, as in the Gd/Y system, a further reduction of *a*- or *b*-axis RKKY interaction is expected in addition to its already short range. For the system with very similar susceptibilities, as in the Dy/Y or Er/Y SL's, the effect of inhomogeneity is less important. In ferromagnetic systems, it is possible that the effects of other interactions, specifically isotropic interactions such as the dipolar interaction, may play an important role in determining the interlayer coupling in the SL's.

The crude model described above predicts the range and the anisotropy of the interaction rather well. In particular, the range of 100–150 Å along the *c* axis and the anisotropy by a factor 10 are in satisfactory general agreement with the observation for the Dy/Y system. The interaction volume for each magnetic ion is evidently an ellipsoid with a long axis of ~ 240 Å along **c** and, at most, 30 Å along **a** and **b**. This volume is approximately 10^5 Å^3, corresponding to $\sim 10^3$ neighbors. It readily accounts for the observed magnetic ordering in dilute Y alloys containing only a few atomic percent of magnetic species.[15] As pointed out earlier, similar features in the susceptibilities and matrix elements of Dy and Y may help to mitigate inaccuracies of the model. Finally, the lack of coupling along **a** and **b** further reinforces earlier beliefs that the observed long range of the coupling in *c*-axis SL's is *not* an artifact due to unknown structural flaws such as strong alloying. The *b*- and *c*-axes samples were grown under very similar conditions, and the interfaces of the *b*-axis samples are, if anything, less perfect than those of the *c*-axis samples.

We note that, for the very different case of an isotropic exchange interaction, there will be a large reduction in

the interlayer coupling for a- or b-axis samples relative to their c-axis counterpart when the magnetic layer separation is greater than the spiral wavelength. In this case, an amplitude cancellation occurs especially near a symmetry direction because the interaction is summed along the spiral direction which is perpendicular to the growth axis. No such cancellation occurs when the magnetic spiral is perpendicular to the growth plane. This cancellation effect should not be relevant in the present case because the long-range c-axis coupling derives from anisotropic peaks in $\chi(\mathbf{q})$.

B. Magnetoelastic effects

The magnetization curves in Fig. 7 and the critical-field curves in Fig. 8 reveal the absence of a first-order transition from the helical to the ferromagnetic phases for temperatures down to 5 K. In bulk Dy, the first-order transition in a field persists up to 130 K.[16] In the presence of a field, the transition in SL's is initiated at H_c and takes place continuously (or possible stepwise) through intermediate "fan" states to attain the pure ferromagnetic state at a much higher saturation field H_f. Like the turn angle ω in Fig. 6, both H_c and H_f for the b-axis samples vary less with temperature than in the bulk and in comparable c-axis samples,[3] but approach the bulk values near T_N. Kitano and Nagamiya[17] show that the large basal plane anisotropy energy in bulk Dy below about 130 K suppresses the intermediate "fan" state and causes a first-order transition from helical to ferromagnetic states. At higher temperature, the rapid decrease in sixfold anisotropy gives rise to a "fan" state. Magnetostriction competes with the epitaxial constraint to cause similar effects[18,19] because a thick substrate can clamp the strain of the epilayer crystal and hence greatly modify its magnetostriction. As a consequence, the critical field H_c (Fig. 8) and turn angle ω (Fig. 6) resemble bulk values only within a very narrow temperature range near the Néel point where spins are nearly random, making magnetic zone, magnetostriction, and anisotropy effects minimal.

In mean-field theory for $4f$ magnetism, the free-energy driving ferromagnetism is given by[19]

$$f_d=\Delta f_{\rm ex}+\Delta f_{\rm me}+\Delta f_{\rm an}+\mu H \ . \tag{6}$$

Here $f_{\rm ex}$ is the exchange energy [which favors antiferromagnetic (AF) arrangements], $f_{\rm me}$ is the magnetoelastic energy [which generally prefers the ferromagnetic (F) phase], and $f_{\rm an}$ is the crystal-field anisotropy. In each case, $\Delta f=f(\mathrm{F})$-$f(\mathrm{AF})$ determines the difference of the free energies between the F and AF arrangements. The discussion that follows neglects the sixfold anisotropy. We assume that the Zeeman energy is only important in the ferromagnetic phase. Then, a spontaneous ferromagnetic transition occurs when f_d is negative, as in bulk Dy. In the spiral phase, f_d is positive, and a critical external magnetic field H_c is required to induce spin alignment. Thus, with $f_d=0$ at the phase boundary, Eq. (6) can then be rewritten as

$$\Delta f_{\rm ex}=-\Delta f_{\rm me}+\mu H_c \ , \tag{7}$$

where μ is the temperature-dependent magnetic moment.

The exchange energy between conduction electrons and the localized $4f$ spins in RE's arises from the long-range oscillatory exchange interactions. Together with small perturbations from magnetoelastic effects, it determines the wave vector of the magnetic order.[19] The period of the magnetic order at the onset of AF ordering is determined by FS effects, specifically the peaks in $\chi(\mathbf{q})$ resulted from the nesting features in the FS discussed in Sec. III A combined with the magnetocrystalline anisotropy; its temperature dependence, on the other hand, arises from the superzone gaps and possible nonlinear effects.[2] In bulk materials, the widening of this AF energy gap, as the temperature is lowered, destroys large segments of the nonmagnetic FS, particularly the webbing features that drive the long-range ordering, and hence modifies the magnetic structure. Attempts have been made to include the effects of the distorted FS in a free-electron band calculation of ω,[20] but these effects are known to fall outside the linear regime and cannot be accounted for by free-electron band models.[2] In films and SL's, the bulk FS's are further distorted, but the magnetic zone effects appear to be much less pronounced, especially for a- and b-axes samples, as indicated by the weak temperature dependence of ω.

We consider a phenomenological approach in which the exchange energy is parametrized by the effective exchange constants between planes together with experimental values of ω. By using a three-layer interaction model,[19] the exchange energy may conveniently be evaluated as

$$\Delta f_{\rm ex}=\sigma^2 J_1(1-\cos\omega)^2/2\cos\omega \ . \tag{8}$$

J_1 is temperature independent and $\sigma=\mu/\mu_{\rm sat}$ or its equivalent with J_2 held constant. For Dy, the saturation moment $\mu_{\rm sat}$ is approximately $10.6\mu_B$. Here, the exchange barrier $\Delta f_{\rm ex}$ depends on a single parameter J_1 which can be determined from the values of ω and H_c below T_N, where magnetoelastic and anisotropy effects are negligible [see Eq. (7)], and the observed values of ω.[19,21] In this paper however, we have evaluated J_1 near T_c to produce the known bulk exchange barrier consistent with the magnetoelastic energy (see the Appendix). Figure 10 shows temperature dependences of the barrier height, calculated for b-axis samples with $J_1=240$ J/cm^3, assuming (8) to hold at all temperatures, and with the measured values of ω (Fig. 6). A similar analysis with J_2 assumed constant gives the same result to within 10% (dotted lines in Fig. 10). The values for bulk Dy are also shown for comparison. Note that we have neglected the magnetoelastic contribution to Eq. (8) and, as we have shown in the Appendix for bulk Dy, the magnetoelastic contribution to J_1 is about 1 J/cm^3.

This phenomenological description of the exchange energy can be summarized as follows. Near the Néel point, only the pure exchange minimum is observed, so all samples have similar barrier heights. As the temperature is lowered, however, the exchange barrier is modified as an-

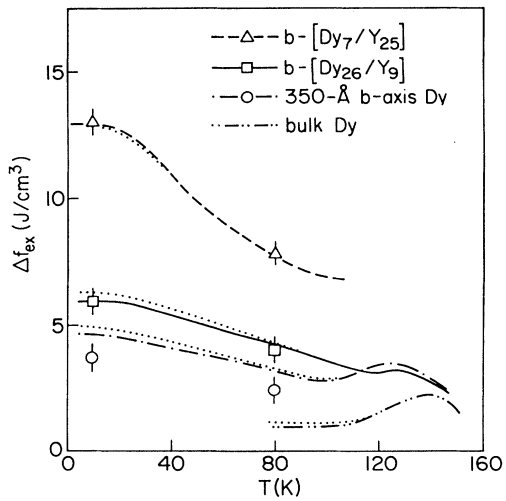

FIG. 10. Temperature-dependent exchange barrier for the *b*-axis samples and for the bulk Dy. Lines indicate the calculated barrier height using the experimental turn angles and with J_1 held constant at 240 J/cm^3, and dotted lines shows the calculated exchange barrier with J_2 held constant at -80 J/cm^3. The variation of the barrier height at a given temperature for the same sample constitute a less than 10% difference between calculations. Points represent the right-hand side of Eq. (7) that is the sum of the magnetoelastic driving force described in the text and the Zeeman energy from the H_c data (see, e.g., Fig. 8).

tiferromagnetic superzone gaps change the ratio $J_1/4J_2$, which we have modeled by using the empirical values of ω. As evidenced by its strongly temperature dependent ω, superzone effects cause bulk Dy to have the lowest exchange barrier at low temperature. On the other hand, in the strained systems including alloys, the epitaxial constraint seems to resist those energy-gap effects that lead to a temperature dependent ω.

A quantitative description of the transition requires careful attention to the magnetoelastic term on the right-hand side of Eq. (7). Perfect epitaxy constrains the growth planes of Dy and Y that are fully coherent. The result of minimizing the magnetoelastic free energy with respect to Cartesian strains subject to this constraint is given by[22]

$$\begin{aligned}\bar{f}_{\rm me} &= -\tfrac{1}{2}\sum_{\mu,\nu}\hat{c}^{(\alpha)}_{\mu\nu}\bar{\varepsilon}_{\mu\mu}\bar{\varepsilon}_{\nu\nu}+\text{const} \\ &= -\tfrac{1}{2}\sum_{\mu}\hat{K}^{(\alpha)}_{\mu}\bar{\varepsilon}_{\mu\mu}+\text{const}\ . \end{aligned} \tag{9}$$

Here, for the αth growth direction, the effective elastic constant in the growth plane (i.e., $\mu,\nu\neq\alpha$) is

$$\hat{c}^{(\alpha)}_{\mu\nu}=c_{\mu\nu}+r_\alpha(\tilde{c}_{\mu\nu}-\tilde{c}_{\mu\alpha}\tilde{c}_{\alpha\nu}/\tilde{c}_{\alpha\alpha})$$

with $c_{\mu\nu}$ and $\tilde{c}_{\mu\nu}$ elastic constants for Dy and Y, respectively, and r_α is the proportion of nonmagnetic material (Y). The $\bar{\varepsilon}_{\mu\mu}$ are the equilibrium strains. Similarly, the effective magnetoelastic coupling constant for this growth plane is

$$\hat{K}^{(\alpha)}_{\mu}=K_\mu+r_\alpha\sum_{\nu(\neq\alpha)}\tilde{\varepsilon}_{0\nu}(\tilde{c}_{\mu\nu}-\tilde{c}_{\mu\alpha}\tilde{c}_{\alpha\nu}/c_{\alpha\alpha})\ . \tag{10}$$

Here, $\tilde{\varepsilon}_{0\nu}$ represents the fractional lattice mismatch without magnetostriction. All the strain variables in Eq. (9) can be measured by conventional scattering techniques and $\Delta\bar{f}_{\rm me}$ can then be calculated using the bulk elastic and magnetoelastic coupling constants $c_{\mu\nu}$, $\tilde{c}_{\mu\nu}$, and K_μ.[22] In this paper we calculate $\Delta\bar{f}_{\rm me}$ by eliminating the equilibrium strains $\bar{\varepsilon}_{\mu\mu}$ from Eq. (9), solving the relation $\sum_\nu\hat{c}^{(\alpha)}_{\mu\nu}\bar{\varepsilon}_{\nu\nu}=\hat{K}^{(\alpha)}_{\mu}$. Lattice clamping is introduced by a lattice mismatch $\tilde{\varepsilon}_{0\nu}$, and an adjustable volume ratio r_α of magnetic to nonmagnetic components.

In earlier work (Ref. 22), Eq. (9) is used to calculate $\Delta\bar{f}_{\rm me}$ for *c*-axis grown Er and Dy samples, and the resulting critical fields agree with the measurements rather well. For *b*-axis Dy samples, lattice clamping from Y is very strong because the substrates are a factor $>10^3$ thicker than the film. The growth plane of the film therefore expands to follow changes of the substrate.[23] This is verified by measurements of *c*-axis expansion in the growth plane for *b*-axis samples, as in the results shown in Fig. 11. In this limit of large r_b, Eq. (9) gives

$$\begin{aligned}\Delta\bar{f}_{\rm me} &= -(1/2c_{11})\Delta(K_2)^2 \\ &\quad -\varepsilon_0\{\Delta K_1+\Delta K_3-[(c_{12}+c_{13})/c_{11}]\Delta K_2\}\ . \end{aligned} \tag{11}$$

Near 0 K, we take $c_{11}=7.7\times10^4$ J/cm^3, $c_{12}=2.5\times10^4$ J/cm^3, $c_{13}=1.9\times10^4$ J/cm^3, $c_{33}=8.5\times10^4$ J/cm^3, and K_1(F)$=266$ J/cm^3, K_2(F)$=-317$ J/cm^3, K_3(F)$=600$ J/cm^3, K_1(AF)$=-24.8$ J/cm^3, K_2(AF)$=-24.8$ J/cm^3, and K_3(AF)$=520$ J/cm^3 determined for bulk Dy. The inplane lattice strains ε_0 are estimated from the measured *c*-axis lattice constants for samples *A*, *B*, and *C*, to be 0.6%, 1.4%, and 0.3 %, respectively. We therefore find $\Delta\bar{f}_{\rm me}=4.4$, -9.6, and -2.6 J/cm^3, respectively. Similarly, at 80 K, with the bulk values $c_{11}=6.7\times10^4$ J/cm^3, $c_{12}=1.6\times10^4$ J/cm^3, $c_{13}=2.0\times10^4$ J/cm^3, $c_{33}=8.4\times10^4$ J/cm^3, and K_1(F)$=61.4$ J/cm^3, K_2(F)$=-304$ J/cm^3, K_3(F)$=342$ J/cm^3,

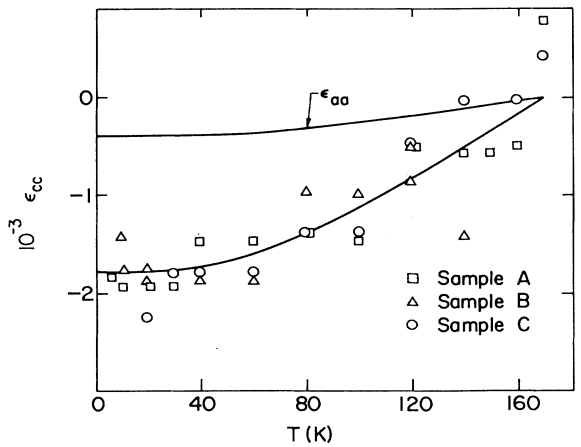

FIG. 11. The temperature variation of the *c*-axis strains for the *b*-axis samples, as determined by neutron scattering. The line shows the corresponding strain for bulk Y (Ref. 24).

$K_1(\mathrm{AF})=-68.5$ J/cm^3, $K_2(\mathrm{AF})=-68.5$ J/cm^3, and $K_3(\mathrm{AF})=223$ J/cm^3, we obtain $\Delta\bar{f}_{\mathrm{me}}=-2.7$, -5.7, and -1.5 J/cm^3, respectively. Of course, these numerical results depend on how the thermal expansion and other parameters are estimated, but one qualitative feature remains valid. For *b*-axis films, the larger the lattice clamping, the bigger the gains in f_{me} and the stronger the tendency to go ferromagnetic from magnetoelastic energy *alone*. For *c*-axis films, on the contrary, stronger clamping leads to less likelihood for a ferromagnetic transition.[22]

To compare this result with the exchange barrier obtained from Eq. (8), we add to the calculated $-\Delta\bar{f}_{\mathrm{me}}$, from Eq. (11), the Zeeman energy μH_c from the critical field data [right-hand side of Eq. (7)]. The resulting values at two different temperatures are shown in Fig. 10. For all the samples, the comparison between the modeled driving force for ferromagnetism and the exchange barrier at the critical phase boundary is well within the uncertainty of the model. The error bars shown in Fig. 10 arise from systematic uncertainties in the critical-field estimates.

The striking agreement between the two sides of Eq. (7) as displayed in Fig. 10 for a wide range of H_c and ω demonstrates internal consistency among observed values of ω, H_c and ε_0. Thus, the parametrization of the exchange barrier via the observed turn angle permits us to quantitatively investigate the energy balance between the different magnetic phases including the anisotropic behavior associated with different growth directions. We summarize the behavior of the magnetic transition in different samples as follows. Lattice clamping evidently suppresses the mechanisms that drive ω toward zero, thereby leaving the exchange barrier at close to its value at T_N. This is accompanied by a relatively small increase in available magnetoelastic energy leaving these systems much harder to magnetize than either *c*-axis samples or bulk Dy, requiring, therefore, a much higher critical field. In the *c*-axis systems, the superzone effects are more effective and, even though the driving force for ferromagnetism decreases with clamping, they are more easily driven to the ferromagnetic phase.

C. Intralayer magnetic coherence

The magnetic phases of Dy discussed in Sec. III B are determined mainly by the competition between the exchange and the magnetoelastic energies. When the helimagnetic phase is preferred, the local energy balance determines characteristics of the magnetic arrangement such as ω. Interfacial roughness, dislocations, and uneven interdiffusion can modify this local energy balance and cause variations in ω which limit the magnetic domain size.

In RE's, the exchange coupling in the basal plane is always ferromagnetic. The strong coupling "locks" each individual *a-b* plane, into a ferromagnetic sheet with very large in-plane domain size. On the other hand, the coupling along the *c* axis is oscillatory, and the energy of the system may be represented by a phenomenological form mostly f_{ex} with magnetoelastic corrections.[25]

$$f\sim J_0(\varepsilon,c)+J_1(\varepsilon,c)\cos\omega+J_2(\varepsilon,c)\cos 2\omega+\cdots . \quad (12)$$

Here, the J's depend on the strain ε and the concentration c if alloying is present. The interlayer turn angle can be determined by minimizing f with respect to ω. Experiments clearly establish that ω depends on both ε and c (Ref. 26) as do the data shown in Fig. 6, particularly the ε dependence. In *c*-axis SL's, both ε and c are periodic along **c** but are uniform along **c** for films. In both cases the spins are periodic along **c** and no loss of coherence is observed with decreasing temperature. Near the interfaces of *a*- or *b*-axes samples, however, ε and c may fluctuate randomly along **c** through the sample, owing to heterogeneities of the materials. This can lead to a position dependence of ω which, we speculate, limits the coherence shown in Fig. 4.

Gradients of ε and c along the growth direction in *a*- and *b*-axis samples should produce a corresponding gradient in ω along the same direction. However, ferromagnetic exchange locks each basal plane. The moments in neighboring planes must then adjust to a new energy minimum that defines a single local ω along **c** within each domain. This local ω is determined by the thickness ratio of the Dy/Y interface layer to the Dy layer itself. Near the Néel point, the values of ω for pure Dy, for the Dy/Y alloy, and for the strained Dy, lie between 42° and 50° and are thus all similar. Therefore, the resulting ω lies in the same range and exhibits relatively small fluctuation. As the temperature is lowered, however, ω for bulk Dy decreases rapidly while that for dilute Dy alloys stays almost fixed; strain can give rise to similar differences. The large changes can obviously increase the fluctuations of ω along **c**. The unexpectedly strong reduction of magnetic coherence in Fig. 4, and its temperature independence at low temperature where ω reaches its smallest value, are both consistent with this interpretation. Furthermore, if fluctuations of ω were mostly interface dependent, thicker Dy layers should have larger values of ξ_c, as is actually observed in the two SL's studied here. Because the 350-Å film was grown at 400 °C, 50 °C higher than the SL's, the interdiffusion layer may be about ten times greater than that in the SL's and the interface-to-Dy layer thickness ratio remains about the same as in sample *A*. This may explain why the behavior of ξ_c in the film is very similar to that in sample *A* (samples *A* and *C* in Fig. 4).

IV. CONCLUSION

In this paper we report the results of experiments that reveal highly orientation-dependent magnetic structures in Dy/Y SL's grown along different crystallographic axes. These consequences of anisotropy in magnetic exchange and magnetoelastic effects are deeply rooted in the RE electronic structure, and derive ultimately from the hcp crystal symmetry.[1,2] A semiquantitative description of the behavior presented here, using bulk properties of pure RE's, is reasonably successful. While a lack of experimental information on the electronic structure and elastic properties of the SL's limits the discussion, there is nevertheless substantial agreement between the phenome-

nological predictions and the experimental observations. Much of the analysis depends on the assumption that individual layers in SL's each respond as they would in bulk RE, modified only by the epitaxial constraint. This leads to the belief that experiments using films can be designed specifically to investigate bulk behavior, such as the spatial form of $J(\mathbf{R})$.

We note finally that the electrons in SL's are, to some degree, shared among neighboring layers owing to the fact that the mean free path may be significantly longer than the layer thickness. Accordingly, they must share a common FS when the electron relaxation is relatively weak, and the magnetic and elastic properties must be altered.[7] Explicit effects due to electron relaxation and superzone formation in metal SL's, and specifically those effects associated with magnetic ordering, have not yet been studied experimentally. One important question that remains to be answered is how two magnetic layers can be coupled by the conduction electrons through Y 120 Å thick when the mean free paths of the electrons involved in transport near the Néel point are known to be less than 100 Å. Band-structure calculations for SL's, when available,[27] and measurements along the lines of the present work may improve the understanding of these interfacial phenomena and the associated magnetic effects.

ACKNOWLEDGMENTS

We thank R.-R. Du for helpful assistance and discussions. This work was supported in part by National Science Foundation (NSF) Grant No. DMR-88-20888 and by the National Institute of Standards and Technology. Use has been made of the facilities of the Materials Research Laboratory, University of Illinois, funeded by the NSF Grant No. DMR-86-12860. One of us (F.T.) thanks the IBM Corporation for partial support during this research.

APPENDIX: THE MAGNETOELASTIC CONTRIBUTION TO THE TEMPERATURE DEPENDENCE OF THE MAGNETIC TURN ANGLE

The ω-dependent total free energy is given by

$$f(\omega)\sim f_{\rm ex}(\omega)+f_{\rm me}(\omega) = \sigma^2 J_1\cos\omega+\sigma^2 J_2\cos(2\omega)+f_{\rm me}(\omega)\ , \qquad \text{(A1)}$$

where the three-layer exchange interaction model is parametrized by J_1 and J_2 (same as $2B_1$ and $2B_2$, respectively, in Refs. 1 and 19). The relationship between J_1 and J_2 is found by minimizing the total free energy with respect to ω:

$$J_1=-4J_2\cos\omega+(1/\sigma^2\sin\omega)\partial f_{\rm me}(\omega)/\partial\omega\ . \qquad \text{(A2)}$$

For bulk Dy, we can evaluate the second term on the right-hand side of Eq. (A2) by using the magnetoelastic energy derived in Ref. 12 in which only the one-ion and two-ion contributions to the magnetoelastic energy are included. We obtain

$$(1/\sin\omega)\partial f_{\rm me}(\omega)/\partial\omega=\tfrac{1}{2}\varepsilon^{\alpha,1}\left[c_{11}^{\alpha}\lambda_1^{\alpha}+\frac{1}{2\sqrt{3}}c_{22}^{\alpha}\lambda_2^{\alpha}\right]+\frac{\sqrt{3}}{2}\varepsilon^{\alpha,2}\left[c_{11}^{\alpha}\lambda_1^{\alpha}-\frac{\sqrt{3}}{2}c_{22}^{\alpha}\lambda_2^{\alpha}\right]\ , \qquad \text{(A3)}$$

where the equilibrium strains, the elastic and the magnetoelastic constants are all written in terms of the hexagonal modes. With the known bulk values, the calculated magnetoelastic contribution to J_1, $[(1/\sigma^2\sin\omega)\partial f_{\rm me}(\omega)\partial\omega]$, changes from 0 J/cm^3 at T_N to about 1 J/cm^3 above T_c. For ω to change from 43° at T_N to 26° just above T_c, with J_2 held constant at ~ -80 J/cm^3 in order to fit the experiment, J_1 must change from 240 to 290 J/cm^3. The magnetoelastic contribution of 1 J/cm^3 is therefore negligible. By rewriting (A1) as $J_1=-4J_2\cos\omega$, we obtain Eq. (8) of the text.

We finally note that, in determining J_1, we have normalized Eq. (8) to fit the right-hand side of Eq. (7) using bulk values.[1,19] We have specifically favored the fit near bulk T_c in order to produce the known exchange barrier near that temperature. The published J_1 on the other hand, was obtained by normalizing the fit below T_N where magnetoelastic effects are minimal (Refs. 1 and 19). We have obtained a J_1 of 240 J/cm^3 which gives an exchange barrier height of about 1 J/cm^3 just above T_c for bulk Dy. This is required to balance the magnetoelastic energy of about 1 J/cm^3 (Refs. 12 and 21) and a negligible planar anisotropy of about 0.1 J/cm^3 (Ref. 19) if Eq. (7) is to hold for all temperatures, especially at low temperature where magnetoelastic effects are important. This J_1 is larger than the published value of 150 J/cm^3 (Refs. 1 and 19) which gives a barrier height of about 0.6 J/cm^3 above T_c not consistent with the known magnetoelastic data.

[1]B. Coqblin, *The Electronic Structure of Rare-Earth Metals and Alloys: The Magnetic Heavy Rare Earths* (Academic, London, 1977).

[2]A. J. Freeman, in *Magnetic Properties of Rare-Earth Metals,* edited by R. J. Elliott (Plenum, New York, 1972), Chap. 6; B. Coqblin, *ibid.* Chap. 9.

[3]For the Gd/Y system, J. Kwo, D. B. McWhan, and E. M. Gyorgy, L. C. Feldman, and J. E. Cunningham, in *Layered Structure, Epitaxy and Interfaces,* edited by J. H. Gibson and L. R. Dawson (Materials Research Society, Pittsburgh, 1985), p. 509; C. F. Majkrzak, J. W. Cable, J. Kwo, M. Hong, D. B. McWhan, Y. Yafet, J. Wasczak, and C. Vettier, Phys. Rev. Lett. **56**, 2700 (1986). For the Dy/Y system, R. W. Erwin, J. J. Rhyne, M. B. Salamon, J. Borchers, S. Sinha, R. Du, J. E. Cunningham, and C. P. Flynn, Phys. Rev. B **35**, 6808 (1987). For the Er/Y system, J. Borchers, M. B. Salamon, R. Du, C. P. Flynn, R. W. Erwin, and J. J. Rhyne, Superlatt. Microstructures **4**, 439 (1988). For the Ho/Y system, C. F. Majkrzak, D. Gibbs, P. Boni, A. I. Goldman, J. Kwo, M. Hong, T. C. Hsieh, R. M. Fleming, D. B. McWhan, Y. Yafet,

J. W. Cable, J. Bohr, H. Grimin, and C. L. Chien, J. Appl. Phys. **63**, 3447 (1988).

[4]R. Du, F. Tsui and C. P. Flynn, Phys. Rev. B **38**, 2941 (1988).

[5]C. P. Flynn, F. Tsui, and M. B. Salamon, R. W. Erwin, and J. J. Rhyne, J. Phys.: Condens. Matter. **1**, 5997 (1989).

[6]J. J. Rhyne, R. W. Erwin, J. Borchers, M. B. Salamon, R. Du, and C. P. Flynn, J. Appl. Phys. **61**, 4043 (1987); M. Hong, R. M. Fleming, J. Kwo, L. F. Schneemeyer, J. V. Waszcak, J. P. Mannaerts, C. F. Majkrzak, D. Gibbs, and J. Bohr *ibid.* **61**, 4052 (1987).

[7]Y. Yafet, J. Kwo, M. Hong, C. F. Majkrzak, and T. O'Brien, J. Appl. Phys. **63**, 3453 (1988).

[8]D. S. Gornyy and R. M. Al'twoskiy, Fiz. Met. Metalloved. **30**, 87 (1970).

[9]For example, on Au (100) surface, M. A. VanHove, R. J. Koestner, P. C. Stair, J. R. Biberian, L. L. Kesmodel, I. Bastos, and G. A. Somoijai, Surf. Sci. **103**, 189 (1981).

[10]P. Delescluse and A. Masson, Surf. Sci. **100**, 423 (1980).

[11]J. J. Rhyne, in *Magnetic Properties of Rare-Earth Metals,* edited by R. J. Elliott (Plenum, New York, 1972), Chap. 4.

[12]W. E. Evenson and S. H. Liu, Phys. Rev. **178**, 783 (1969).

[13]S. H. Liu, R. P. Gupta, and S. K. Sinha, Phys. Rev. B **4**, 1100 (1971).

[14]T. Kasuya, in *Magnetism IIB,* edited by G. T. Rado and H. Suhl (Academic, New York, London,, 1966), Chap. 3.

[15]J. A. Gotaas, J. J. Rhyne, L. E. Wagner, and J. A. Mydosh, J. Appl. Phys. **61**, 3415 (1987).

[16]M. Akhaven, H. A. Blackstead, and P. L. Donoho, Phys. Rev. B **8**, 4258 (1973).

[17]Y. Kitano and T. Nagamiya, Prog. Theor. Phys. **31**, 1 (1964).

[18]B. R. Cooper and R. J. Elliott, Phys. Rev. **131**, 1043 (1963); **153**, 654(E) (1967).

[19]B. R. Cooper, in *Magnetic Properties of Rare-Earth Methods,* edited by R. J. Elliott (Plenum, New York, 1972), Chap. 2; B. Coqblin, *ibid.* Chap. 7.

[20]For example, H. Miwa, Proc. Phys. Soc. **85**, 1197 (1965).

[21]M. Rosen and H. Klimker, Phys. Rev. B **1**, 3748 (1970).

[22]R. W. Erwin, J. J. Rhyne, J. Borchers, M. B. Salamon, R. Du, and C. P. Flynn, in *Neutron Scattering for Materials Science,* edited by S. M. Shapiro, S. L. Moss, and J. D. Jorgensen, MRS Symposia Proceedings No. 166 (Materials Research Society, Boston, 1989), p. 133.

[23]This has been shown for semiconductors, for example, N. Lucas, H. Zabel, H. Morkoç, and H. Unlu, Appl. Phys. Lett. **52**, 2117 (1988).

[24]R. W. Meyerhoff and Y. F. Smith, J. Appl. Phys. **33**, 219 (1962).

[25]E. W. Lee, Proc. Phys. Soc. **84**, 693 (1964).

[26]H. Umebayashi, G. Shirane, B. C. Frazer, and W. C. Daniels, Phys. Rev. **165**, 688 (1968); H. R. Child, W. C. Koehler, E. O. Wollan, and J. W. Cable, *ibid.* **138**, A1655 (1965).

[27]A recent tight-binding model calculation for the *c*-axis RE/Y SL's by J. B. Xia and Y. C. Chang (unpublished) has revealed a long-range magnetic coherence through Y in quantitative agreement with the discussion in Sec. III A.

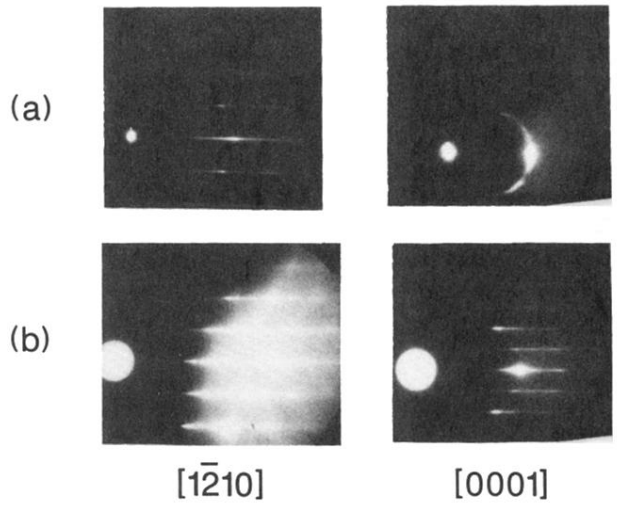

FIG. 1. Typical RHEED pictures for *b*-axis samples: (a) a reconstructed surface showing long streaks along the [1$\bar{2}$10] azimuth and an arc along the [0001] azimuth, and (b) an unreconstructed surface having somewhat shorter streaks along both [1$\bar{2}$10] and [0001] directions.